Journal of Power Sources 198 (2012) 105–111

Contents lists available at SciVerse ScienceDirect

Journal of Power Sources

journal homepage: www.elsevier.com/locate/jpowsour

Short communication

The effect of processing route on sinterability and electrical properties of nano-sized dysprosium-doped ceria

S.A. Acharya*

Department of Physics, Rashtrasant Tukdoji Maharaj Nagpur University, Nagpur, M.S., India

ARTICLE INFO

Article history:
Received 30 June 2011
Received in revised form 9 September 2011
Accepted 23 September 2011
Available online 1 October 2011

Keywords:
Microwave-assisted combustion
Dysprosium-doped ceria
Sinterability
Electrolyte
Solid oxide fuel cell

ABSTRACT

In the present work, the microwave heating (MH) route is used to prepare and sinter dysprosium-doped ceria (DDC) nanopowder, $Ce_{(1-x)}Dy_xO_{2-x/2}$ (x = 0.05–0.25 at.%), and the results are compared with the same composition obtained by conventional heating (CH). The results show that the as-synthesized powders are pure oxides with high crystallinity. The average crystallite size of the MH-DDC samples is approximately 22 nm, while the CH-DDC sample size is approximately 29 nm. The sinterability of the MH samples is greater than that of the CH samples. Microwave sintering produces high-density MH-DDC pellets with fine and almost homogeneous grain-growth and a grain size of 400 nm, while the conventionally densified pellets have non-uniform grains range in size from 1100 to 1400 nm. The electrical properties of the sintered pellets were investigated by impedance spectroscopy. The ionic conductivity of the MH-DDC15 pellet sintered by microwave at 1050 °C for 1 h was determined to be $\sigma_{550\,^\circ C} = 7.42 \times 10^{-2}$ S cm^{-1}, with an activation energy of E_a = 0.86 eV. The pellets that were conventionally sintered at 1300 °C for 5 h were found to have ionic conductivity of $\sigma_{550\,^\circ C} = 9.79 \times 10^{-3}$ S cm^{-1}, with E_a = 1.05 eV. The correlations between the grain, grain boundary relaxation and ion transport mechanism in nanocrystalline electrolyte materials are discussed.

1. Introduction

Solid oxide fuel cells (SOFCs) are solid-state electrochemical devices that convert the chemical energy in fuels directly into electricity with high conversion efficiency and low toxic gas emissions, and they are highly flexible in terms of the fuels they use [1–3]. However, to be economically competitive, it is necessary to lower their operating temperature (below 600 °C) [4]. It has been recognized that decreasing the temperature of the cells depends on high-quality electrolytes with higher oxide ionic conductivity [5]. The research on electrolytes has mainly focused on (i) the use of thin electrolyte films and (ii) the development of highly conducting solid electrolytes using different dopants and co-dopants [6–8]. To realize these requirements, there is a need to (a) introduce new concepts of materials development and processing (b) design systems where a great control over the microstructure can be obtained.

In the last decade, nanocrystalline materials have been widely accepted to have a high potential to meet above mentioned requirements [9–14]. Nano-ionic ceramic oxides display electrical properties that appear to be unique and may lead to applications that are not normally attainable by conventional microcrystalline oxides [15]. The ionic conductivity of nanocrystalline materials has been found to be significantly enhanced compared with that of their microcrystalline equivalents [16–20]. Doped ceria electrolytes have been known to exhibit higher ionic conductivity at relatively lower temperatures compared to yttrium-stabilized zirconia (YSZ), and they have been extensively studied as the most promising electrolyte materials for intermediate temperature SOFCs [21–25]. The ionic conductivity of ceria-based systems has been reported to be an order of magnitude greater than that of YSZ, especially when its nanocrystalline nature is retained [26,27]. However, it has been observed that nanocrystalline ceria can be densified at a much lower temperature because of the high surface energy of the nanoparticles [16,28–30].

In general, the preparation method has a great deal of influence on the microstructure and stability of nanocrystalline ceramic solid solutions. Several synthesis routes have been developed to produce nanocrystalline CeO_2-based powders, such as the precipitation of ceria using ammonia [31], ammonium carbonate [32], hydrazine hydrate [33], sol–gel [34], forced hydrolysis of inorganic salts [35], combustion synthesis [36], and hexamethylenetetramine-based homogeneous precipitation [37]. Very recently, microwave-assisted chemical synthesis routes have emerged as highly controlled methods for the production of nano-sized materials [38].

Recently, samarium- and gadolinium-doped ceria have attracted increasing attention as electrolytes for low-temperature

* Tel.: +91 9372078410; fax: +91 712 2500736.
E-mail address: saha275@yahoo.com

0378-7753/$ – see front matter © 2011 Elsevier B.V. All rights reserved.
doi:10.1016/j.jpowsour.2011.09.087

SOFCs [39–44]. It has been considered that the doped ceria electrolytes exhibited high oxide ionic conductivity as a result of the small association enthalpy between the dopant cation and the associated oxygen vacancies in the fluorite lattice [45]. Accordingly, dysprosium-doped ceria (DDC) has a comparable association enthalpy to that of samarium- or gadolinium-doped ceria electrolytes [46]. Therefore, it is expected that DDC would be a promising solid electrolyte material for applications in low-temperature SOFCs. In the present work, we attempted to prepare nano-crystalline DDC by glycine-nitrate combustion routes. The combustion synthesis was carried out in two ways: (i) conventional heating of the precursor solution at 300 °C and (ii) microwave heating at 400 W. The five different compositions of $Ce_{(1-x)}Dy_xO_{2-x/2}$ (x = 0.05–0.25 at.%) are prepared and characterized by X-ray diffraction (XRD), scanning electron microscopy (SEM), and transmission electron microscopy (TEM). The powders are compacted into pellets and consolidated to a gas-tight density by using a high-temperature muffle furnace and an indigenously built microwave sintering assembly. The microstructures of the sintered pellets are examined by SEM, and their electrical conductivity was measured by AC impedance spectroscopy.

2. Experimental procedure

2.1. Powder synthesis

The nano-sized solid solutions of $Ce_{1-x}Dy_xO_{2-x/2}$ (DDC, x = 0.05–0.25 at.%) were prepared by combustion synthesis routes induced by microwave (MH) and conventional (CH) mode of heating. Table 1 lists the various compositions and their nomenclature used in the present work. Cerium nitrate hexahydrate ($Ce(NO_3)_3{\cdot}6H_2O$), dysprosium nitrate hexahydrate ($Dy(NO_3)_3{\cdot}6H_2O$, 99.99% pure, Aldrich) and glycine nitrate (>99% pure Merck, Mumbai) were used as starting materials. According to stoichiometric analysis, on the basis of the atomic percentage of $Ce_{1-x}Dy_xO_{2-x/2}$, aqueous solutions of ($Ce(NO_3)_3{\cdot}6H_2O$) and ($Dy(NO_3)_3{\cdot}6H_2O$) were mixed initially in a quartz beaker. Glycine nitrate was added to the mixed metal nitrate solution. In each case the glycine nitrate/metal nitrate molar ratio was maintained at 1.

The aqueous redox solutions containing metal nitrate and glycine nitrate were introduced into a multimode microwave oven with a chamber size of 360 mm × 210 mm × 430 mm and operated at 2.45 GHz. The maximum deliverable power output was 1.2 kW. The samples were prepared at different values of microwave power. As the sample began to boil in the oven, the froth ignited and caught fire within 1 min. An off-white colored foamy ash powder was formed after the combustion. The foam was then lightly ground in a silica mortar with a porcelain pestle to obtain a fine powder. The as-synthesized light yellow powder was used for further studies and characterization. For the conventional heating induced combustion synthesis, the procedure that was followed was similar to what has been previously reported [47,48].

Table 1
List of various compositions and their nomenclature.

Composition	Nomenclature for mode of heating used for synthesis and sintering	
	Microwave	Conventional
CeO_2	MH-DDC0	CH-DDC0
$Ce_{0.95}Dy_{0.05}O_{2-\delta}$	MH-DDC05	CH-DDC05
$Ce_{0.90}Dy_{0.10}O_{2-\delta}$	MH-DDC10	CH-DDC10
$Ce_{0.85}Dy_{0.15}O_{2-\delta}$	MH-DDC15	CH-DDC15
$Ce_{0.80}Dy_{0.20}O_{2-\delta}$	MH-DDC20	CH-DDC20
$Ce_{0.75}Dy_{0.25}O_{2-\delta}$	MH-DDC25	CH-DDC25

2.2. Characterization

Room temperature powder XRD was carried out on the as-prepared MH and CH samples for phase identification and for the crystallite size estimation, using a Bruker D8 Advance X-ray diffractometer with CuKα radiation at a scanning rate of 1° min^{-1}. The morphology of the samples was observed using a scanning electron microscope (SEM, JEOL-6360) and transmission electron microscope (TEM, Technai 20G^2) operated at an accelerating voltage of 200 keV using carbon-coated Formvar grids. The sample was prepared by dispersing the nanostructures in N,N-dimethylformamide (DMF) using ultrasonication. The calcined powders were well milled in an agate mortar. The powder was pressed uniaxially under 250 MPa to form green pellets of a 10 mm diameter and an approximately 1 mm thickness. The pressed pellets were sintered by microwave and by the conventional method. The microwave sintering assembly was designed in-house and was fabricated by modifying a domestic microwave oven. For conventional sintering, a locally made, high-temperature muffle furnace was used. The sintering conditions were optimized for temperature and time for both heating methods. The best sintering results were obtained by microwave at 1050 °C for 1 h and by the conventional apparatus at 1400 °C for 5 h with a heating rate of 5° min^{-1}. The sinterability of the samples was quantitatively studied from the graphical correlation of the sintering temperature and relative density. The relative density was calculated as the ratio of the experimental to theoretical density ($d_{rd} = d_{ex}/d_{th}$) for all the compositions and all synthesis conditions. The theoretical density d_{th} was calculated as the ratio of the mass of the atoms in the unit cell to the volume of the unit cell by the lattice parameter, and the sintered density d_{ex} was determined using the Archimedes method.

The microstructures of the sintered specimens were observed by SEM. The impendence spectra were investigated in the temperature interval from 200 to 700 °C and in the frequency range from 5 Hz to 13 MHz by an HP-4191 impedance analyzer. Platinum electrodes were sputtered onto either side of the sintered DDC pellets.

3. Results and discussion

The powder XRD of the as-prepared MH-DDC15 and CH-DDC15 samples (representative composition) are shown in Fig. 1. The XRD patterns clearly indicate the formation of the cubic phase, with homogeneous mixtures of Ce^{4+} and Dy^{3+} in the fluorite structure. The broad nature of the XRD peaks (Fig. 1) indicates the fine size of the crystallites of the developed DDC15 solid solution. The average particle size was measured by using the Scherrer equation:

$$t = \frac{0.9l}{b\cos q} \quad (1)$$

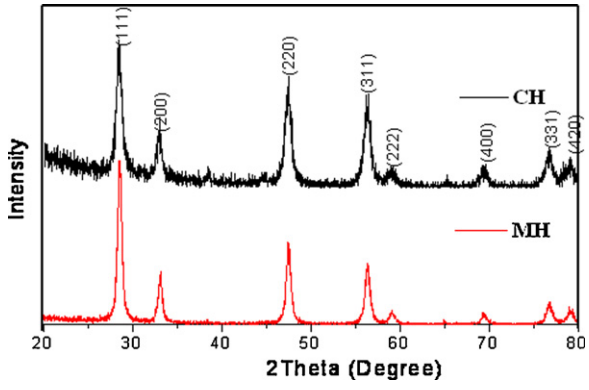

Fig. 1. XRD patterns of as-prepared MH and CH-DDC15 powder.

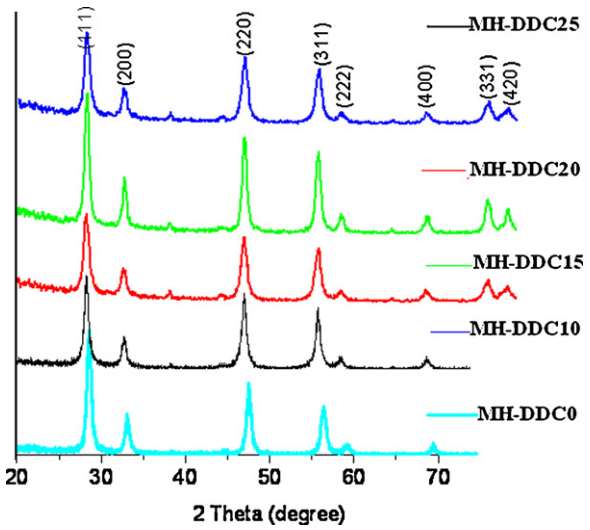

Fig. 2. XRD of as-synthesized MH-DDC samples for different composition.

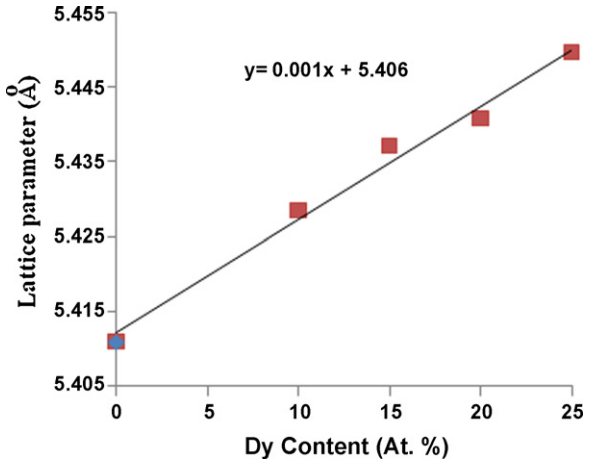

Fig. 3. Lattice parameter of doped ceria as a function of Dy content in MH-DDC samples.

t is the average crystalline size, λ is the wavelength of X-rays, θ is the position of the reflection in XRD pattern in degrees, and β is the integral breadth of reflection (in radians 2θ) located at 20 and often calculated by using a solid reference standard, i.e., $\beta^2 = \beta_s^2 - \beta_r^2$. The average particle size of the MH and CH powders were found to be approximately 22 and 29 nm, respectively. The XRD patterns of the MH-DDC samples at different compositions are illustrated in Fig. 2. Analysis of the XRD for the different

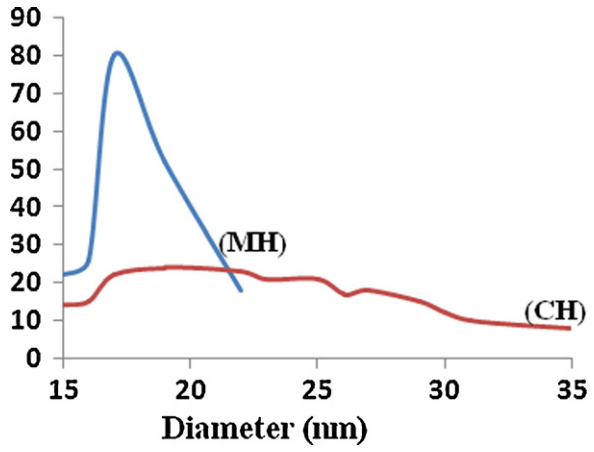

Fig. 5. Particle-size distribution from SEM images of MH and CH samples.

compositions showed that the obtained powders were of a single phase, independent of the dopant concentration in the range investigated. The calculation of the cell parameters on the basis of the XRD results (Fig. 3) confirms their linear dependence on the atomic percentage of x of Dy^{3+} ions; this result suggests the formation of a complete solid solution in the given compositional range. The cubic ceria lattice was observed to expand with increasing Dy ion concentration. Thus, doping with the larger-sized ($r_{Ce^{4+}} = 0.97\,Å$; $r_{Dy^{3+}} = 1.027\,Å$) Dy^{3+} ions and increasing the dopant concentration will continue to increase the cell parameters. The lattice parameter of the doped ceria was in accordance with Vegard's law. The same trend is observed in the CH-DDC samples, as well.

The microstructures of the as-prepared MH-DDC15 and CH-DDC15 samples are shown in Fig. 4A and B, respectively. The SEM images of both samples exhibit an average grain size of less than 100 nm. The grain size distribution for both samples was determined by manual image analysis of approximately 200 particles. As the particles of both samples were of a nearly round shape, particle sizes could be determined by matching the digital pixel scale with the diameter. The obtained data from the image analysis were quantitatively studied by plotting a graph of particle size versus the number of particles (Fig. 5). The average particle size was determined from the arithmetic mean of the particles sizes and its standard deviation. The particle-size distribution obtained from SEM for the CH sample has an arithmetic mean particle size and standard deviation of 27 and 33 nm, respectively. For the MH sample, the SEM indicates that the size distribution is both smaller and narrower than for the CH sample, which has an arithmetic mean particle size and standard deviation of 17 nm and 9 nm, respectively. This allows the prediction that the size distribution is more fine and uniform in the MH material than in the CH samples. The

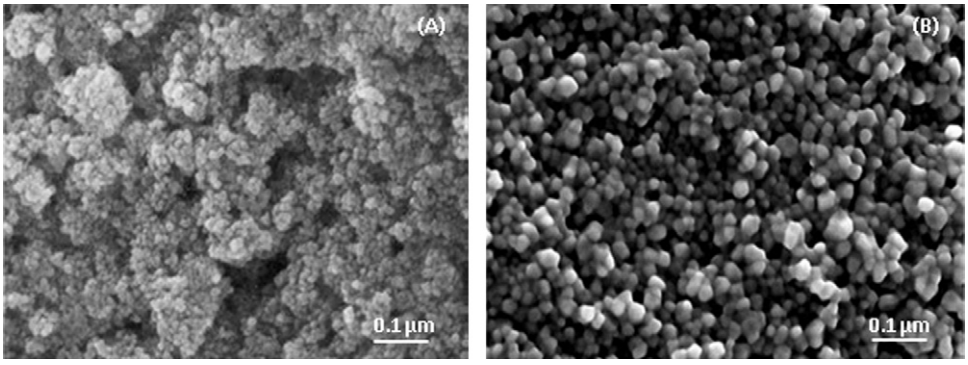

Fig. 4. SEM micrographs of (A) MH-DDC15 and (B) CH-DDC15 samples.

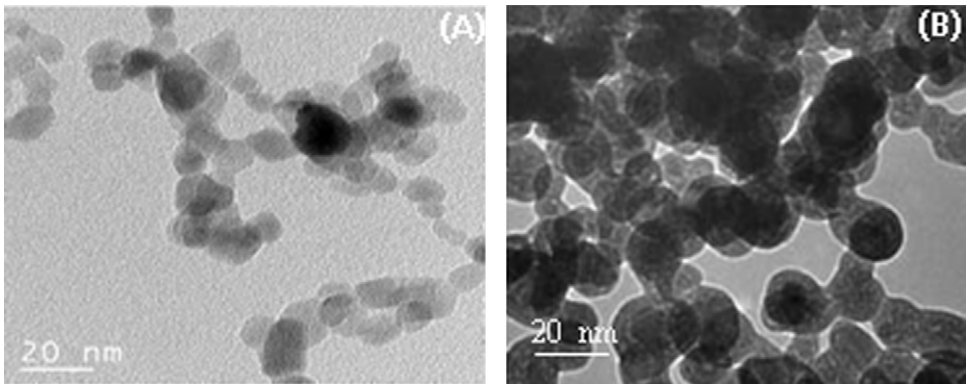

Fig. 6. TEM images of (A) MH-DDC15 and (B) CH-DDC15 samples.

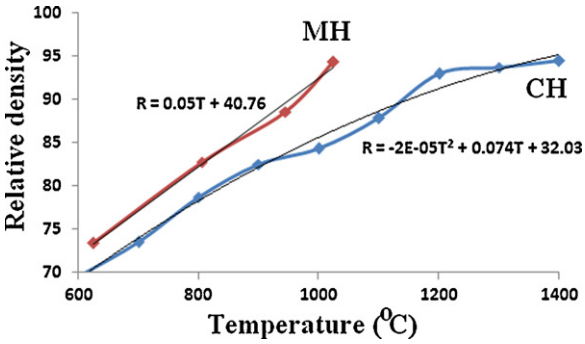

Fig. 7. Sinterability of MH-DDC15 and CH-DDC15 samples.

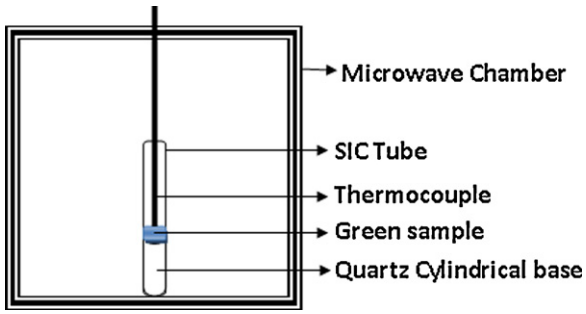

Fig. 9. Schematic view of microwave sintering assembly.

TEM images (Fig. 6A and B) confirm the nanoscale size distribution of the crystallites of both samples. For the MH (Fig. 6A) sample, the average particle size was observed to be approximately 17 nm, while for the CH sample (Fig. 6B), it was approximately 27 nm. From the TEM results, it can be determined that agglomeration and non-uniformity in the particles size distribution are more prominent in the CH samples than in the MH samples.

The sinterability of the MH-DDC15 and CH-DDC15 samples is shown in Fig. 7, and all compositions of MH and CH samples are displayed in Fig. 8A and B for meaningful comparisons. The sintering assembly used for microwave sintering is shown in Fig. 9. The green pellet was placed on a cylindrical base made of quartz. The cylinder was inserted in a SiC tube of nearly 3 cm diameter and 15 cm length. To measure the temperature, a shielded S-type thermocouple was used and was inserted into the tube from the upper side of the oven, where a leakage-proof hole was made for the insertion of the thermocouple. The thermocouple was placed in contact with the surface of the pellet. The MH samples were sintered at the 700, 800, 900 and 1000 W power levels of the microwave with an irradiation time of 1 h at each power. The corresponding temperatures were measured to be 650, 830, 970 and 1050 °C, respectively. For conventional sintering, green pellets of DDC were placed in heating boat, which were introduced into a high-temperature muffle furnace. The CH samples were sintered at temperatures from 600 to 1400 °C in the muffle furnace, for 5 h at each temperature.

The MH samples were sintered to almost 95% of the theoretical density by microwave at very low temperature (1050 °C) and in a very short time of 1 h, in contrast to CH, which required 1300 °C for 5 h to achieve compaction to 94% of the theoretical density (Fig. 7). To understand the role of the mode of heating on the sinterability, temperature versus relative density data of MH and CH samples were fitted by regression analyses. The sinterability data of the MH-DDC15 samples are found to be linear, described by the relation

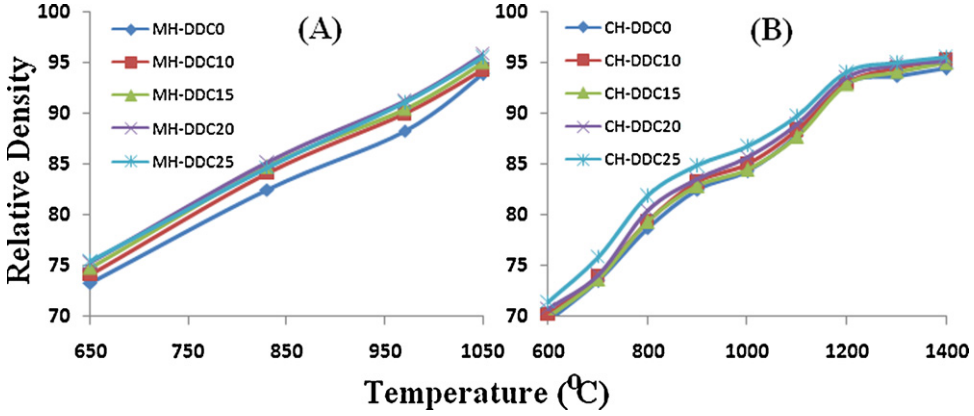

Fig. 8. Sinterability of MH-DDC and CH-DDC samples at different compositions.

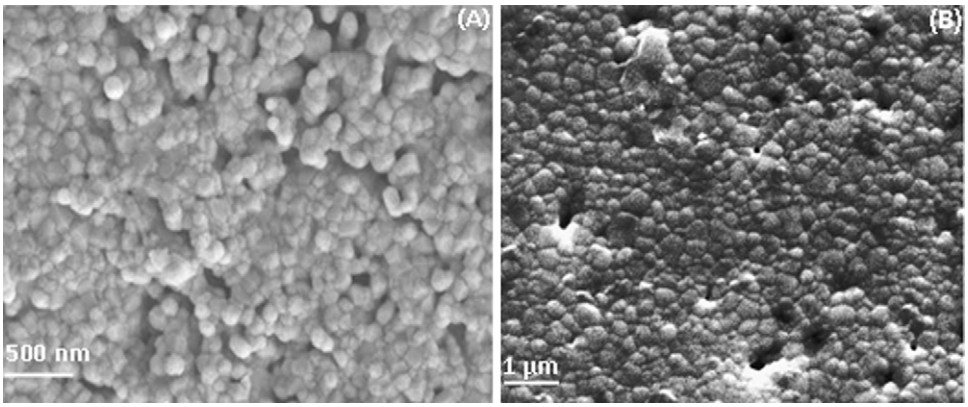

Fig. 10. SEM images of green pellets (A) MH-DDC15 and (B) CH-DDC15.

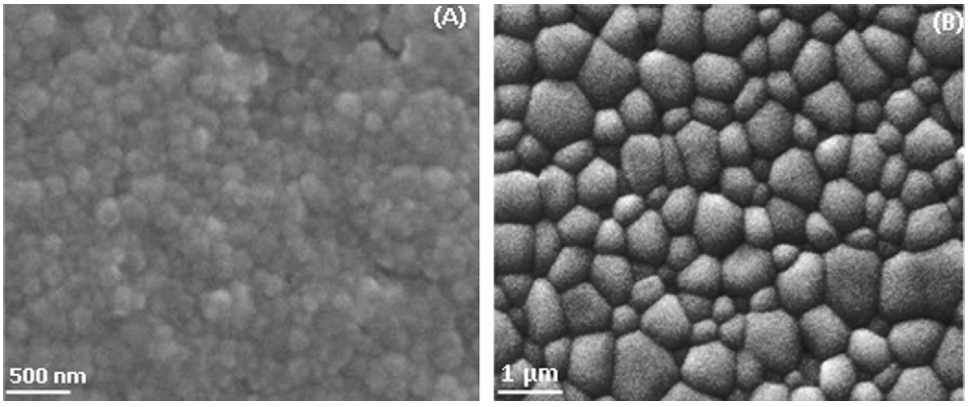

Fig. 11. SEM images of sintered pellets (A) MH-DDC15 (at 1050 °C) and (B) CH-DDC15 (at 1400 °C).

$R = 0.042T + 47.19$; whereas the CH-DDC15 samples data are described by the non-linear relation $R = -2E{-}05T^2 + 0.074T + 32.03$. This fitting clearly indicates that the sinterability of MH sample exhibits a linear relation between the relative density and temperature, whereas the CH sample exhibits a nonlinear relation. From Fig. 8, it can be observed that almost all compositions show the same sinterability trends. SEM images of green pellets of MH-DDC15 and CH-DDC15 are shown in Fig. 10A and B, and highly density compacted pellets are shown in Fig. 11A and B, respectively. The grain size of the MH and CH pellets before sintering is found (Fig. 10A and B) to be approximately 40 and 70 nm, respectively; however, after sintering and attaining a gas-tight density, the grain size is observed (Fig. 11A and B) to increase to approximately 400 nm for the microwave sintered (at 1050 °C) pellet and 1100 nm for the conventionally sintered (at 1400 °C) pellet, respectively. The microwave sintered pellet achieved near-theoretical density by raising its grain-size approximately 10 times above that of the green pellet. The conventionally sintered pellet also becomes highly consolidated by increasing its grain-size to approximately 15 times more than the green pellet. The microwave sintered pellet was found to undergo linear and rapid densification with a slow rate of grain growth, maintaining near-homogeneity. The conventional route was observed to follow a nonlinear process of densification, causing a grain growth non-uniform. Porade [49] has also studied the microwave and conventional sintering of bulk ceramics and observed a critical enhancement of the densification rate with controlled grain-growth and homogeneity maintained in the grains.

The complex impedance plots of the MH-DDC15 and CH-DDC15 samples at 300 °C are shown in Fig. 12. Two separate semicircles are observed within the measured frequency range. The first depressed semicircle in the high frequency region corresponds to the grain interior resistance, and the second depressed semicircle represents the grain boundary. The grain boundary depressed semicircle is larger than the grain interior depressed semicircle for both samples. The same impedance plot trends are exhibited (Fig. 13) by the CH samples in the high temperature range (400–700 °C), but for MH samples a single depressed semicircle was observed. The relaxation frequency of the grain may be too high (>13 MHz) to be shown in the spectra, so only the grain boundary response was observed in the high temperature range.

To understand the role of relaxation frequencies in the grain and grain boundary conductivity, the impedance loss spectra are studied at various temperatures for MH-DDC15 (Fig. 14). Two relaxation peaks are observed at higher and lower frequencies (Fig. 14) for the low-temperature range (300–420 °C). For the high-temperature

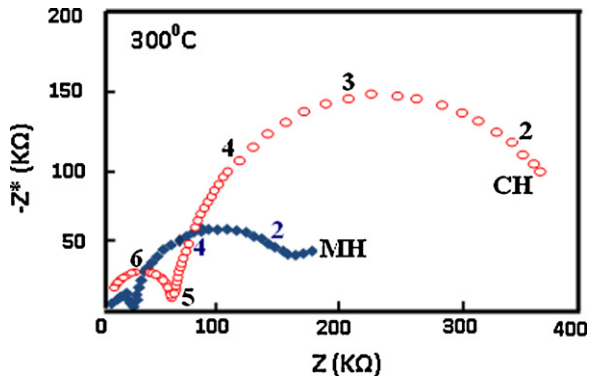

Fig. 12. Complex impedance plot of MH-DDC15 and CH-DDC15 samples at 300 °C.

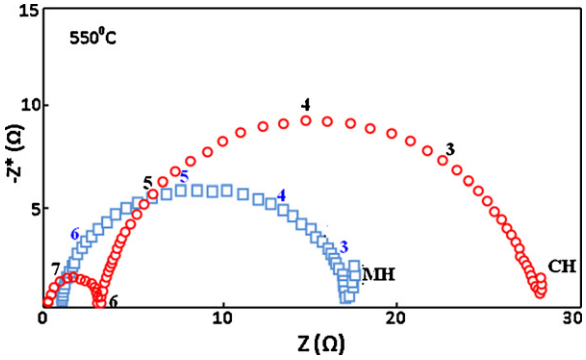

Fig. 13. Complex impedance plot of MH-DDC15 and CH-DDC15 samples at 550 °C.

range (420–600 °C), a single relaxation peak was detected on the lower-frequency side. The relaxation peaks at higher and lower frequencies have been found to correspond to the grain interior and grain boundary conduction, respectively [20,50]. The impedance loss spectra confirmed the relaxation of charge carriers, along with conduction in the grain interior and boundaries. The relaxation peaks appeared to be shifted towards the higher frequency side with increasing temperature. The relaxation frequency was the macroscopic parameter that helped to predict the electrical processes occurring in the material. The results are interpreted to indicate that higher values of relaxation frequency correspond to lower charge carrier relaxation times in their respective region. This relationship initiates a faster charge relaxation process and indicates that the relaxation of oxygen ions is faster in the grain than at the grain boundary and that the relaxation rate increases with increasing temperature. The comparative impedance loss spectra of MH-DDC15 and CH-DDC15 at 340 °C are displayed in Fig. 15. They indicate that the relaxation frequency corresponding with the grain and grain boundary of MH sample is greater than the corresponding frequency for CH. This difference confirms that the relaxation of oxygen ions is faster at the grain and grain boundary of the MH samples than the CH ones. The size of the grains was found to be for a controlling factor for the relaxation of the oxygen ion.

From the comparative impedance graphs (Figs. 12 and 13), it can be observed that the grain boundary resistance was less in MH sample than in CH. This difference is noteworthy, as the grain boundary plays a vital role in determining the total ion conductivity

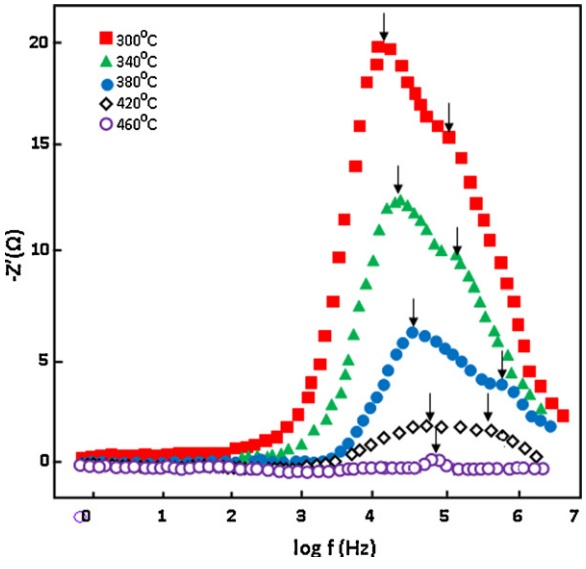

Fig. 14. Impedance loss spectra of MH-DDC15 samples at different temperatures.

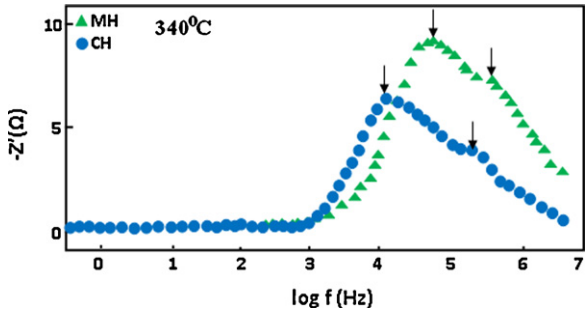

Fig. 15. Impedance loss spectra of MH-DDC15 and CH-DDC15 samples at 340 °C.

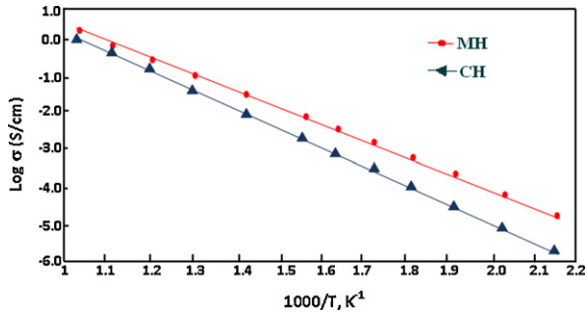

Fig. 16. Arrhenius plot for total ionic conductivity of MH-DDC15 and CH-DDC15 samples.

in polycrystalline ceramics. The difference in the grain boundary resistance observed for MH and CH was mainly attributed to the difference in grain size. The decrease in grain boundary resistance with increasing grain size for the MH sample indicates an enhancement of the oxide-ionic conductivity via grain boundaries. Bellino et al. [51] have also observed the decrease in grain boundary resistance with grain size for nanostructured Y and Sm-doped ceria.

It has been reported by many investigators that the main contribution of the conductivity of ceria-based oxides in air is oxide ion conductivity; hence, the measured conductivity in air of the given MH and CH materials are considered to be solely attributable to the oxide ion conductivity. The measured conductivity of the studied MH and CH samples and all compositions of MH are displayed in Figs. 16 and 17, respectively, in the Arrhenius plot. An analysis of the data plotted in Fig. 16 reveal that the mobility of the oxide ions was higher in the small-grained MH samples (<500 nm) than in the larger-grained CH ones (>1000 nm). Thus, one may assume that the reasons for this enhancement lie in homogeneous grains of the microwave sintered MH samples; they give rise to an ordered structure of the oxygen vacancies within the grain. The ordering of the oxygen vacancies within the grain expands the conduction pathway across the grain boundary. This explains

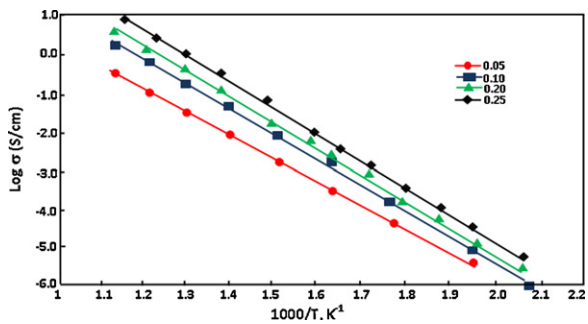

Fig. 17. Arrhenius plot for total ionic conductivity of MH-DDC for different composition.

the increase in conductivity of the MH samples in comparison to the CH ones. The effects of the processing route on the sinterability and its influence on the microstructure and conduction mechanism at the atomic scale have been also shown by Mori et al. [52,53]. The maximum conductivities with minimum activation energies are observed for MH-DDC15 sintered at 1050 °C for 1 h, for which $\sigma_{550\,^\circ C} = 7.42 \times 10^{-2}\,S\,cm^{-1}$, $E_a = 0.86$ eV, and CH-DDC15 at 1300 °C for 5 h, for which $\sigma_{550\,^\circ C} = 9.79 \times 10^{-3}\,S\,cm^{-1}$, $E_a = 1.05$ eV. The ionic conductivity obtained for the MH samples is much higher compared with the earlier reported conductivity ($4.2 \times 10^{-3}\,S\,cm^{-1}$) for DDC10 by Bautista et al. [54].

4. Conclusion

The influence of the processing methodology on the sinterability and conduction properties in the Dy-doped ceria (DDC) system was systematically studied in the present work. The conventional and microwave modes of heating were used to synthesize and sinter DDC systems with different compositions. The as-synthesized MH samples were observed to be spherical, with nearly uniformly distributed nanoparticles and an average particle size of approximately 17 nm. The CH samples were found to be highly agglomerated, with particles having an average size of approximately 27 nm. Densely sintered bodies (more than 95% of theoretical density) with almost homogeneously developed grains with an average size of 400 nm were obtained by microwave sintering, while for conventional sintering samples, the average grain size was observed to be approximately 1100 nm. The structural morphology and conductivity properties of the MH samples were compared with those of the CH samples. The ionic conductivity of the pellets sintered by microwave at 1050 W for 1 h was observed to be $\sigma_{550\,^\circ C} = 7.42 \times 10^{-2}\,S\,cm^{-1}$, $E_a = 0.86$ eV, while for conventionally sintered pellet at 1300 °C for 5 h, it was found to be $\sigma_{550\,^\circ C} = 9.79 \times 10^{-3}\,S\,cm^{-1}$, $E_a = 1.05$ eV. The dielectric relaxation of the grain and the grain boundary were found to be dependent on their size and associated with the charge conduction mechanism. This study underscores the potential of microwave-assisted synthesis and sintering of nanocrystalline dysprosium-doped ceria powders for applications as electrolytes in IT-SOFCs.

Acknowledgement

This work was funded by Department of Science and Technology, New Delhi through Fast Track Scheme.

References

[1] N.Q. Minh, Journal American Ceramic Society 76 (1993) 563–588.
[2] S.P.S. Badwal, K. Foger, Ceramic International 22 (1996) 257–265.
[3] T. Hibino, A. Hashimoto, T. Inoue, J. Tokuno, S. Yoshida, M. Sano, Science 288 (2000) 2031–2033.
[4] D.J.L. Brett, A. Atkinson, N.P. Brandon, S.J. Skinner, Chemical Society Review 37 (2008) 1568–1578.
[5] T. Mori, Y. Wang, J. Drennan, G. Auchterlonie, J.G. Li, T. Ikegami, Solid State Ionics 175 (2004) 641–649.
[6] S.C. Singhal, Solid State Ionics 135 (2000) 305–313.
[7] J.W. Fergus, Journal of Power Sources 162 (2006) 30–40.
[8] J.G. Li, Y. Wang, T. Ikegami, T. Ishigaki, Solid State Ionics 179 (2008) 951–954.
[9] Y.P. Fua, C.H. Lin, C.W. Liu, K.W. Tay, S.B. Wen, Journal of Power Sources 159 (2006) 38–41.
[10] B. Rambabu, E.S. Ghosh, E.H. Jena, Journal of Material Science 41 (2006) 7530–7536.
[11] S. Surble, G. Baldinozzi, M. Dollé, D. Gosset, C. Petot, G. Petot-Ervas, Ionics 14 (2008) 33–36.
[12] Y.P. Fu, Ceramic International 34 (2008) 2051–2057.
[13] A.K. Baral, V. Sankaranarayanan, Applied Physics Letter 94 (2009) 074101–74103.
[14] D.P. Coll, G.C. Mather, Solid State Ionics 181 (2010) 20–26.
[15] P. Kuppuswami, K. Mutthukkumaran, R. Divakar, R. Kesavamoorthy, E. Mohandas, S. Selladurai, Ionics 13 (2007) 343–348.
[16] H.L. Tuller, Solid State Ionics 131 (2000) 143–157.
[17] T. Mori, T. Kobayashi, Y. Wang, J. Drennan, T. Nishimura, J.G. Li, H. Kobayashi, Journal of American Ceramic Society 88 (2005) 1981–1984.
[18] X. Sha, I. Lu, X. Huang, J. Miao, Z. Ding, X. Xin, W. Su, Journal of Alloys and Compounds 428 (2007) 59–64.
[19] E. Rossinyol, E. Pellicer, A. Prim, S. Estrade, J. Arbiol, F. Pairo, A. Carnet, J.R. Morante, Journal of Nanoparticles Research 10 (2008) 369–375.
[20] A.K. Baral, V. Sankaranarayanan, Applied Physics A 98 (2010) 367–373.
[21] Y. Liu, S. Zha, M. Liu, Chemistry of Materials 16 (2004) 3502–3506.
[22] T. Ishihara, T. Shibayama, M. Honda, H. Nishiguchi, Y. Takita, Chemical Communication (1999) 1227–1228.
[23] T.-H. Yeh, C.-C. Chou, Physica Scripta T129 (2007) 303–307.
[24] S.W. Zha, C.R. Xia, G.Y. Meng, Journal of Power Sources 115 (2003) 44–48.
[25] M.R. Kosinski, R.T. Baker, Journal of Power Sources 196 (2011) 2498–2512.
[26] B.C.H. Steele, Solid State Ionics 129 (2000) 95–110.
[27] J. Hormes, M. Pantelouris, G.B. Balazs, B. Rambabu, Solid State Ionics 136 (2000) 945–954.
[28] Y.M. Chiang, E.B. Lavik, I. Kosacki, H.L. Tuller, J.Y. Ying, Applied Physics Letters 69 (1996) 185–187.
[29] A. Tschope, J.Y. Ying, H.L. Tuller, Sensors and Actuators B 31 (1996) 111–114.
[30] S. Basu, P.S. Davi, H.S. Maiti, Journal of Materials Research 19 (2004) 3162–3171.
[31] J. Van Herle, T. Horita, T. Kawada, N. Sakai, H. Yokokaya, M. Dokiya, Ceramic International 24 (1998) 229–241.
[32] J.G. Cheng, S.W. Zha, J. Huang, X.Q. Liu, G.Y. Meng, Materials Chemistry and Physics 78 (2003) 791–795.
[33] R.O. Fuentes, R.T. Bakers, International Journal of Hydrogen Energy 33 (2008) 3480–3484.
[34] V. Briois, C.E. Williams, H. Dexpert, F. Villain, B. Cabane, F. Deneuve, C. Magnier, Journal of Materials Science 28 (1993) 5019–5031.
[35] H. Xu, H. Yau, Z. Chen, Solid State Science 10 (2008) 1179–1184.
[36] P.L. Chen, I.W. Chen, Journal of American Ceramic Society 76 (1993) 1577–1583.
[37] G.B. Jung, T.J. Huang, M.H. Huang, C.L. Chang, Journal of Materials Science 36 (2001) 5839–5844.
[38] Y.P. Fu, C.H. Lin, C.W. Liu, K.W. Tay, S.B. Wen, Journal of Power Sources 159 (2006) 38–41.
[39] C. Milliken, S. Guruswamy, A. Khandkar, Journal of Electrochemical Society 146 (1999) 872–882.
[40] C. Milliken, S. Guruswamy, A. Khandkar, Journal of American Ceramic Society 85 (2002) 2479–2486.
[41] D. Hirabayashi, A. Tomita, T. Hibino, M. Nagao, M. Sano, Electrochemical Solid-State Letter 7 (2004) A318–A320.
[42] K. Kudo, H. Obayashi, Journal of Electrochemical Society 123 (1976) 415–419.
[43] Y.J. Leng, S.H. Chan, S.P. Jiang, K.A. Khar, Solid State Ionics 170 (2004) 9–15.
[44] A. Tomita, D. Hirabayashi, T. Hibino, M. Nagao, M. Sano, Electrochemical Solid-State Letter 8 (2005) A63–A65.
[45] J. Kilner, Solid State Ionics 8 (1983) 201–207.
[46] V. Butler, C.R.A. Callow, B.E.F. Fender, J.H. Harding, Solid State Ionics 8 (1983) 109–113.
[47] K. Singh, S.A. Acharya, S.S. Bhoga, Ionics 12 (2006) 295–301.
[48] K. Singh, S.A. Acharya, S.S. Bhoga, Ionics 13 (2007) 429–434.
[49] W. Porade, Material Processing Research 55 (1990) 49.
[50] A. Kumar, I. Manna, Physica B 403 (2008) 2298–2305.
[51] M.G. Bellino, D.G. Lamas, N.E.W. de Reca, Advanced Functional Materials 16 (2006) 107–113.
[52] T. Mori, J. Drennan, Journal of Electroceramic 17 (2006) 749–757.
[53] T. Mori, R. Buchanan, D.R. Ou, F. Ye, T. Kobayashi, J.D. Kim, J. Zou, J. Drennan, Journal of Solid State Electrochemistry 12 (2008) 841–849.
[54] C.S. Bautista, A.J.D. Santos-Garcia, J.P. Martinez, J.C. Vazquez, Solid State Ionics 181 (2010) 1665–1673.